Residual NAPL Morphology Effects on Electrical Resistivity: Insights From Micromodel Displacement Experiments and Pore Network Simulations

Siyuan Qiang, Xiaoqing Shi, André Revil, Xueyuan Kang, Yuanyuan Liu, Jichun Wu

Water Resources Research

RESEARCH ARTICLE
10.1029/2022WR033233

Residual NAPL Morphology Effects on Electrical Resistivity: Insights From Micromodel Displacement Experiments and Pore Network Simulations

Siyuan Qiang[1], Xiaoqing Shi[1], André Revil[2], Xueyuan Kang[1], Yuanyuan Liu[1], and Jichun Wu[1]

[1]Key Laboratory of Surficial Geochemistry of Ministry of Education, School of Earth Sciences and Engineering, Nanjing University, Nanjing, China, [2]Université Grenoble Alpes, Université Savoie Mont Blanc, CNRS, UMR CNRS 5204, EDYTEM, Le Bourget du Lac, France

Key Points:

- Non-aqueous phase liquid (NAPL) trapped in dead ends of porous space has little effect on bulk resistivity
- Relationship between the bulk resistivity and Euler characteristic of partially saturated pore network is determined by NAPL wettability
- A power-law relationship is found between the Archie's saturation exponent and NAPL ganglia size

Correspondence to:
X. Shi,
shixq@nju.edu.cn

Citation:
Qiang, S., Shi, X., Revil, A., Kang, X., Liu, Y., & Wu, J. (2022). Residual NAPL morphology effects on electrical resistivity: Insights from micromodel displacement experiments and pore network simulations. *Water Resources Research*, *58*, e2022WR033233. https://doi.org/10.1029/2022WR033233

Received 11 JUL 2022
Accepted 7 DEC 2022

Abstract Characterizing residual non-aqueous phase liquids (NAPLs) in porous media is essential for designing contaminated site remediation strategies. The direct current resistivity method is increasingly being used at sites contaminated by NAPLs, which uses the Archie's second law to connect NAPL saturation with the resistivity of porous media. A power-law relationship connecting the phase morphology measured by Euler characteristic with resistivity has also been observed at the pore-scale. Because these relationships are limited for porous media with specific wettability, previous research works have demonstrated deviations from Archie's second law in both the laboratory and field experiments. To evaluate the effects of residual NAPL morphology with different wettability on bulk resistivity, we developed two 2D-micromodels and measured their electrical resistivity and phase morphology during phase displacement under laboratory-controlled conditions. Furthermore, pore network simulations of a variety of conditions were performed in absence of surface conduction. Results show that NAPL distributed in dead ends of the pore space has limited influence on bulk resistivity since they do not control the current path and voltage distribution. The correlations between resistivity index and Euler characteristic are determined by NAPL ganglia size and pore throat width. A power-law relationship is found between the Archie's saturation exponent and the average size of the residual NAPL ganglia, indicating that this exponent can be interpreted as the rate of change of the pore water connectivity with saturation. These insights provide a physical framework connecting the morphology and wettability of the NAPL ganglia with the Archie's saturation exponent.

Plain Language Summary Petrophysical relationships can relate the non-aqueous phase liquids (NAPLs) saturation with subsurface resistivity, which help us to characterize the underground contaminants. However, researchers often encountered deviations from widely adopted petrophysical relationships that link the electrical resistivity with NAPL saturation because they neglect or wrongly predict the effect of NAPL morphology on resistivity. In our study, we systematically explored the mechanism behind the impact of NAPL morphology on electrical resistivity by micromodel experiments and pore network simulation.

1. Introduction

Groundwater contamination caused by non-aqueous phase liquid (NAPL) is becoming a major environmental threat (Kang et al., 2020; National Research Council, 2013). To design efficient remediation strategies at the field-site scale, high-resolution characterization of NAPL distribution at the pore-scale is essential. After being released in the subsurface, free-phase NAPL often persists as disconnected residual ganglia or pools (Dekker & Abriola, 2000) under the control of both gravity and capillary force (Al-Raoush, 2009). The variable release histories and wettability of the porous media also result in different morphologies of the residual NAPL (Dwarakanath et al., 2002). Figure 1 shows a sketch of possible morphologies for residual NAPL ganglia in the pore space. These residual NAPL ganglia may pose as long-term source of groundwater contamination due to their low solubility. Both the dissolution behaviors and the longevity of NAPL source zone are strongly determined by their morphology (Sahloul et al., 2002).

A variety of methods have been used for NAPL source zone characterization. Intrusive drilling or sampling can provide direct measurements of NAPL saturation. However, these sampling methods often suffer from poor spatial resolution. Geophysical methods can provide non-intrusive spatialized data sets (e.g., Slater & Binley, 2021). In

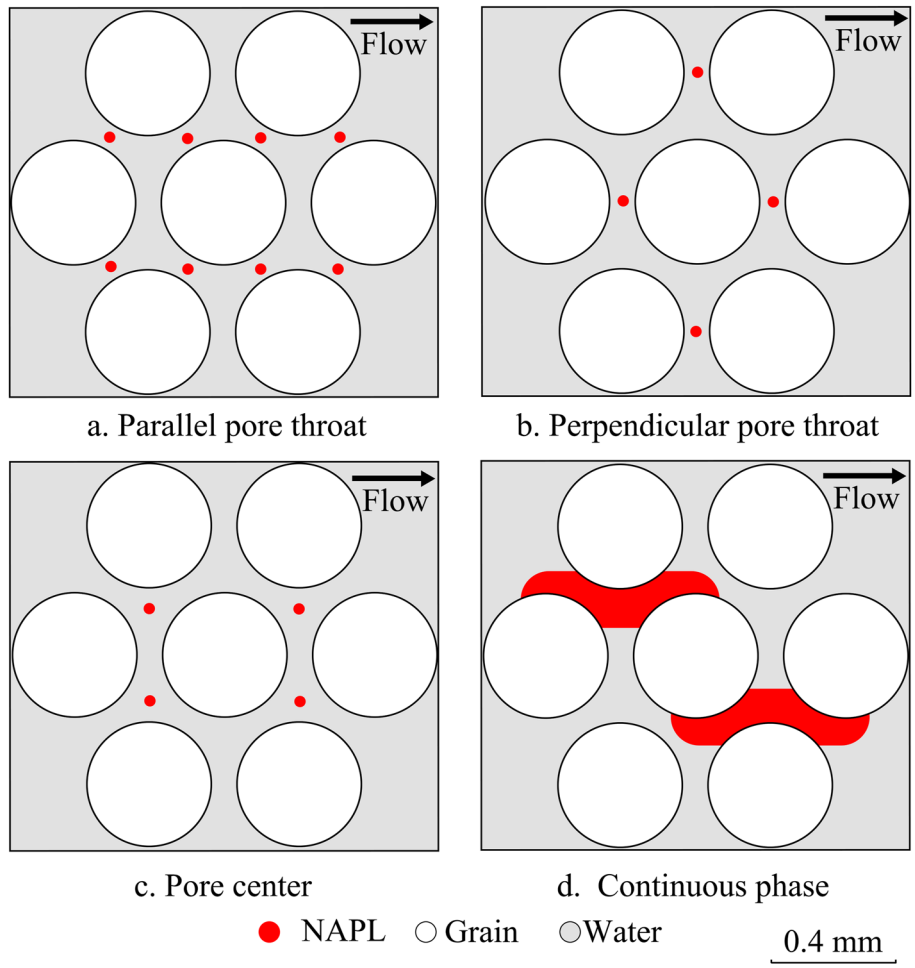

Figure 1. Sketch of possible distribution morphologies for residual non-aqueous phase liquid ganglia in the pore space: (a) Parallel to the flow direction. (b) Perpendicular to the flow direction. (c) In the pore center. (d) As a continuous phase through several pores.

particular, the direct current (DC) resistivity method has become widely used in mapping NAPL contamination due to its low cost and high sampling density (e.g., Daily et al., 1995; Deng et al., 2017; Kang et al., 2018) as well as its extension in terms of induced polarization (IP) (Johansson et al., 2015; Revil et al., 2011; Schmutz et al., 2010).

As the mixture of porous medium and NAPL is not or minimal conductive when NAPL persists as macroscopic pools, we focus here on the influences of the morphology of NAPL ganglia on the electrical resistivity ρ at the pore-scale. The most frequently used petrophysical model to link NAPL saturation with electrical resistivity is the formulation proposed by Waxman and Smits (1968). This model assumes two parallel conductors in porous media, including the bulk conductivity and surface conductivity σ_S (conductivity $\sigma = 1/\rho$):

$$\sigma(S_w) = \frac{\sigma_w}{F} S_w^{\,n} + \sigma_S(S_w) \tag{1}$$

where $\sigma(S_w)$ (S m^{-1}) is the bulk conductivity of the porous material at pore water saturation S_w, σ_w (S m^{-1}) denotes the conductivity of the pore water, F (dimensionless) is the formation factor, $F = \phi^{-m}$ where ϕ (dimensionless) is the porosity and m (dimensionless) denotes the cementation or first Archie exponent, n is the Archie's saturation exponent also called the second Archie's exponent (Archie, 1942), and σ_S represents the surface conductivity contributed by the counterions in the electrical double layer adjacent to the grain and NAPL ganglia surface (Bücker et al., 2017; Wang & Revil, 2020).

The resistivity index RI (dimensionless) is defined as the ratio of the conductivity of porous media at water-saturated to partial water-saturated conditions:

$$RI = \frac{\sigma(S_w = 1)}{\sigma(S_w)} = \frac{\sigma_w + F\sigma_S(S_w = 1)}{\sigma_w {S_w}^n + F\sigma_S(S_w)} \tag{2}$$

The Archie's saturation exponent n is determined by the phase morphology in the pore network (Glover, 2017). Previous studies have shown that field and laboratory experiments often encountered deviations in the Archie's saturation exponent in oil-wet conditions due to the variation of the underlying pore-scale morphology of fluids (Liu et al., 2018; Montaron, 2009). In looking at these works, care should be taken in checking that surface conductivity has been properly accounted for (Niu et al., 2016; Revil et al., 2017). The contribution of surface conduction should be considered when estimating the Archie's saturation exponent. When surface conductivity σ_S is negligible, we obtain:

$$RI = {S_w}^{-n} \tag{3}$$

However, under field situations, the surface conductivity σ_S could not be ignored or even be dominant (Revil & Glover, 1998; Revil et al., 2017; Singha & Gorelick, 2006). The IP method could be used to estimate surface conductivity from the normalized chargeability of porous media (Revil, 2012; Weller et al., 2013). But reliable IP measurements often require a complex electrode system (Zimmermann et al., 2008), which is challenging to implement on the glass-made micro pore model. Therefore, we focus exclusively on DC resistivity in this study, because it is one of the most widely used geophysical techniques and easier to measure (Binley & Kemna, 2005). The influence of surface conduction on the overall resistivity would not be considered.

To describe the resistivity of partially saturated rocks, effective medium theories (Bruggeman, 1935) and percolation theory (Stauffer & Aharony, 2018) are used to develop specific petrophysical models. The effective medium theories estimate the conductivity of porous media by considering the microstructure in a way of averaging (Cosenza et al., 2009). In percolation theory, the conductivity problem can be treated by percolation theory in the absence of surface conductivity, which leads to (Montaron, 2009; Sahini & Sahimi, 1994):

$$RI = \left(\frac{1 - S_{wc}}{S_w - S_{wc}}\right)^{\mu} \tag{4}$$

where S_{wc} is the residual water saturation defined in the permeability expression of the water phase. μ is a critical exponent for the electrical conductivity, which is defined in terms of the fractal dimension in 2D and 3D. Recently, two important parameters, "Water connectivity index" (Montaron, 2009) and "Wettability index" (Newgord et al., 2019, 2020), are further introduced as an extended interpretation of Equation 4 to quantify phase morphology in the pore space.

Nevertheless, these petrophysical models are limited in applicability because these parameters such as n and S_{wc} are difficult to determine empirically (Scholz et al., 2015). The uncertainties of the petrophysical models caused by the competing properties of pore fluids and the effects of phase morphology on resistivity may lead to biased estimation of water saturations in field applications (Tso et al., 2019). Scholz et al. (2012) and Liu et al. (2018) have proposed a power-law relationship between the measurement of phase morphology and the resistivity index, which is independent of these petrophysical parameters. In the absence of surface conductivity, the relationship can be written as:

$$RI = \left(\frac{1 - \chi_0}{N}\right)^{\alpha} \tag{5}$$

where χ_0 is the Euler characteristic (dimensionless) of the conducting phase, N represents the number of grains in the porous media, α is a free parameter. The Euler characteristic represents the connectivity of a specific phase in the pore network and is defined as the difference between the number of connected components of each phase (Armstrong et al., 2019; Mecke & Arns, 2005; Scholz et al., 2012). For porous media at partial water saturation, the Euler characteristic of pore water is defined as the number of connected water phases minus the number of disconnected residual NAPL and solid phases. Figure 2 shows the corresponding Euler characteristics of several pore space sketches. Compared with the water saturation S_w, the Euler characteristic is more intuitive to reveal the relationship between the electrical resistivity and phase morphology. Equation 5 has been proven

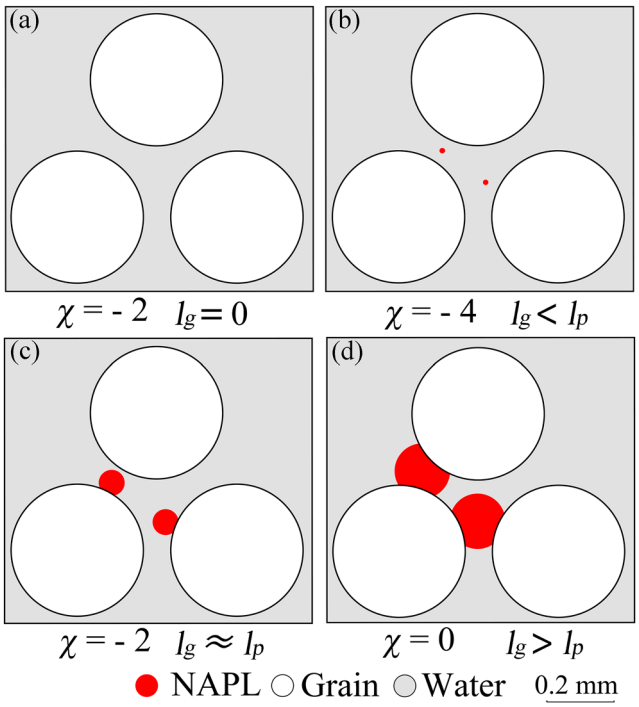

Figure 2. Sketch of residual non-aqueous phase liquid (NAPL) ganglia in the pore space and the corresponding Euler characteristic χ. Here l_g is the diameter of NAPL ganglia, l_p is the minimum width of the pore throat.

for water-saturated 2D grain models (Armstrong et al., 2019). However, Liu et al. (2018) found that this power-law relationship only works in oil- or intermediate-wet (IW) porous media. Similarly, Mustofa et al. (2022) demonstrated no specific relationship between the Euler characteristic and resistivity index in some wetting conditions in 3D columns. These findings indicate that the applicability of this power-law relationship seems to vary with the wettability of porous media.

A visible experimental setup for porous media is crucial to study the pore-scale properties such as Euler characteristics. Many laboratory experiments with geophysical measurements have been conducted in columns (Mendieta et al., 2021; Song et al., 2022) or sandbox/tanks (Deng et al., 2018; Kang et al., 2018; Power et al., 2015). These experimental setups can provide satisfactory data quality but lack good image quality for visibility, which is not applicable to studying the microscopic properties of porous media in this study. Microfluidic experiments have been widely used to study pore-scale phenomenon due to their excellent visibility and controllability (Lan et al., 2022). A number of pore-scale studies experiments have focused on the relationship between the electric properties of porous media and its geometric properties (Sun et al., 2021), wettablilities (Grattoni & Dawe, 1995; Kozlov et al., 2012), and precipitates caused by chemical reactions (Izumoto et al., 2022). However, to the best of our knowledge, no experimental study of the power-law relationship between resistivity and Euler characteristic have been conducted on porous media with different wettability at partial saturation.

In this work, we used 2D glass-etched micromodels with different wettabilities to investigate the impact of residual NAPL ganglia morphology on the Archie's second law. Through NAPL displacement experiments and pore network simulations, we investigated the effect of the position and size of the residual NAPL ganglia on bulk resistivity. Based on the analysis of phase morphology, we further discussed underlying physical properties controlling the Archie's saturation exponent n, which can be interpreted as the rate of change of the pore water connectivity with saturation.

2. Materials and Methods

2.1. Experimental Setup

We designed a 2D glass microfluidic chip with homogeneous cylindrical solid grains of radius $r = 0.2$ mm (Park et al., 2021) and pore throat width $l_p = 0.07$ mm (Figure 3). The micromodel was fabricated by thermally bonding a flat bottom plate with a top plate, which had acid-etched pore networks and holes for inlet and outlet. The pore area was 20 mm × 9.95 mm with a porosity of 0.37. The depth of the pore network was 0.02 mm (Rangel-German & Kovscek, 2006).

The experimental system (Figure 4) consisted of a syringe pump (LSP01-2A, Longerpump), a charge-coupled device (CCD) camera (Alta U2, Apogee) for extensive range imaging, a microscope (CX31, Olympus) for localized imaging, and a resistivity measuring instrument (SIP-LAB, Radic-Research). The system provides detailed phase morphology and simultaneous electrical resistivity measurements.

2.2. Experimental Procedure

The NAPL used in this work is nonpolar mineral oil (Paraffin, CAS:8020-83-5, Aladdin), which can be easily manipulated by displacement rate and wetting conditions due to its differentiated viscosity and surface tension compared to water (Du et al., 2020; Zhang et al., 2020). After fabrication, one of the two glass micromodels was fully saturated with a hydrophobic agent (Nanofluorosilicon polymer, Weiwang) and aged for 10 hr to make it hydrophobic. The contact angle of pore water with the internal surface of this micromodel was measured by

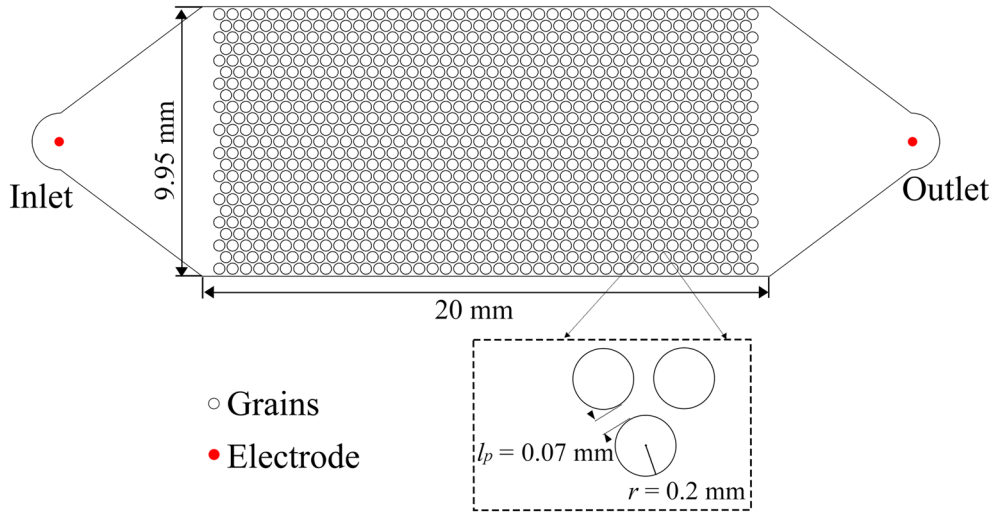

Figure 3. Sketch of the 2D micromodel. The red dots represent the position of the electrodes.

treating a glass plate with the same procedure, the result was 80°–100° and indicated an IW condition (Kovscek et al., 1993). These two wettablities did not cover all wetting conditions, but could produce sufficiently different NAPL phase distributions in the pore space (Liu et al., 2018). Before experiments, the untreated water-wet (WW) and IW micromodel were cleaned by injecting sodium dodecylbenzenesulfonte (CAS: 25155-30-0, Aladdin), ethyl alcohol (CAS: 64-17-5, Macklin), and deionized water in sequence to remove organic and inorganic components. The micromodel was initially saturated with mineral oil dyed by Oil-Red-O (CAS: 1320-06-5, BOSF). The NaCl solution with a conductivity of 0.76 S/m was then injected at 5 and 3 μl/min for two experiment groups, respectively to acquire data corresponding to different displacement rates.

The Euler characteristic and electrical resistivity were measured every 3 s during the displacement process. The Euler characteristics of pore water were calculated by the MATLAB function named "regionprops" (Jing et al., 2017). We used a 2-point probe method (Wei & Llle, 1991) with a 100 Hz, 1 V sinusoidal signal for resistivity measurements. To ensure good electrode contacts, needles coated with tin (diameter = 1 mm) were inserted into the inlet and outlet hole of the micromodel. Fluids could flow through the needles while a cupreous socket soldered on the needles connected it with the electrical connector from the resistivity measuring instrument. The tested contact resistance of the two electrodes only accounts for around 0.06% of the total resistance at relatively high water saturation levels (>0.6). To demonstrate the reliability of the electrodes, NaCl solutions with electrical conductivity ranging from 0.03 to 1.4 S/m at 25°C were injected into the micromodel, the measured conductivity

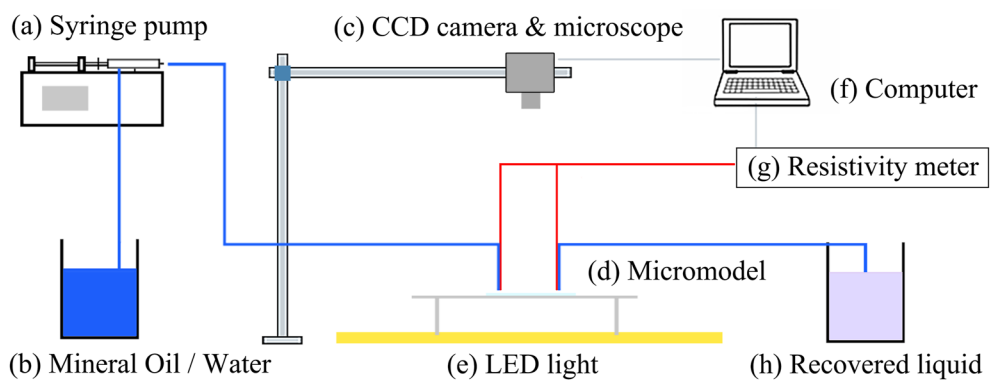

Figure 4. Sketch of the two-phase flow visualization and resistivity measurement system, which consists of (a) syringe pump (LSP01-2A, Longerpump), (b) fluids, (c) CCD camera (Alta U2, Apogee) for extensive range imaging and microscope (CX31, Olympus) for localized imaging, (d) micromodel in Figure 3, (e) LED light, (f) computer for data collection, (g) resistivity meter (SIP-LAB, Radic-Research) and (h) recovered fluid collection system.

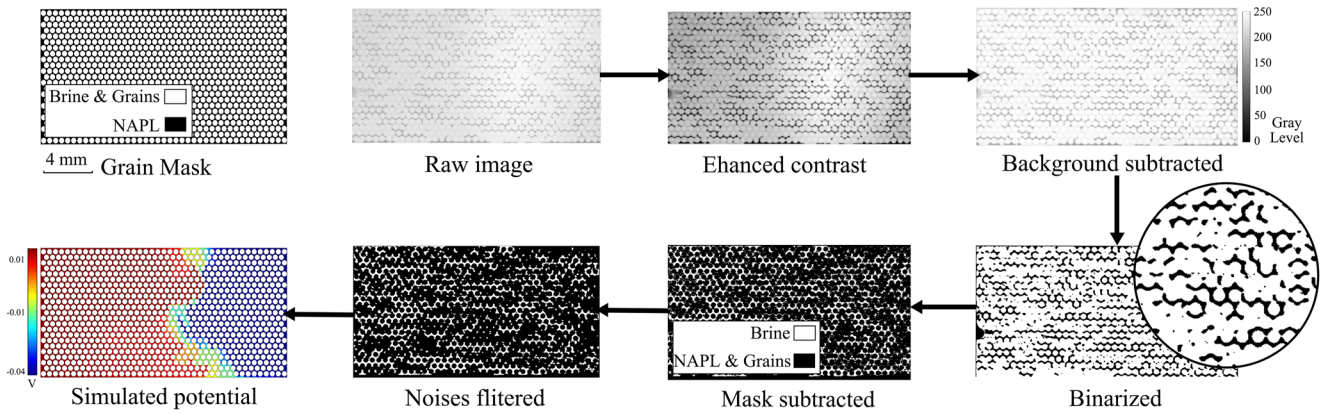

Figure 5. Sketch of the processing procedure of images taken from CCD camera. Note that the images are eventually binarized into conducting and non-conducting phases. The final image shows a simulated electrical potential distribution.

honors the Archie's first law $\sigma\,(S_w = 1) = \sigma_w \phi^m$. The coefficient of determination R^2 between the measured and predicted apparent resistivity reached the highest value 0.9986 for $m = 1.768 \pm 0.03$.

Some repeatability issues can be attributed to the experimental errors introduced by subtle changes with the experimental setup. Indeed, slight variations or disturbances in the pore network may lead to measurable changes in NAPL migration and distribution during NAPL displacement (Yang et al., 2021) even when the experimental conditions are nearly the same. As a result, this small change in NAPL distribution further influences the measurement of the measured resistivity itself. We carried out a series of experiments under a combination condition of two wettabilities and displacement rates. Numerical simulations under these controlled and uncontrolled ideal conditions were also performed to investigate the relationship between the morphology of the NAPL phase and bulk resistivity at the pore-scale.

2.3. Image Processing

The workflow of CCD image processing is shown in Figure 5. We used ImageJ® (Schneider et al., 2012) and codes written in MATLAB (Higham & Higham, 2016) to perform the postprocessing of the images from the CCD camera. First, the "Enhanced Local Contrast" and "Subtract background" plugins in ImageJ® were utilized to enhance the visibility of the NAPL phase and to diminish the influence of uneven background light. The images were then binarized into black (NAPL phase) and white (water phase and grains) with a threshold selected using the "im2bw" function of MATLAB based on Otsu's method (Otsu, 1979). This approach is used to select the aforementioned threshold by minimizing the intraclass variance of the thresholding black and white pixels. Finally, a grain mask taken from a micromodel that was fully saturated with NAPL was subtracted from the image to remove the grains from the white area. As the measurement of Euler characteristic is inherently troubled with the occurrence of isolated pixels resulting from imaging processing (Armstrong et al., 2019; Liu et al., 2017), we used a 2D median filtering function "medfilt2" in MATLAB to remove the isolated noise pixels in the final image. Each output pixel during the filtering contains the median value in a 3-by-3 neighborhood around the corresponding pixel in the input image (Lim, 1990). Images taken from the microscope were not processed to preserve the original NAPL morphology.

2.4. Numerical Methods

The electrical resistivity of the micromodel was simulated with the finite element method with COMSOL Multiphysics® (version 5.4). We built a 2D pore network using the same structures as the experimental micromodel (Figure 3). The grid size in the numerical model matches the pixel size of the CCD images. No electrical double layer was considered in the simulations (Revil et al., 2014) on the surface of the grain and/or NAPL ganglia surface in the simulations. Thus, the surface conduction related to the electrical double layer was completely discarded and the pore network was converted to a single heterogeneous conductor. All resistivity variations were solely caused by changes in the bulk conductivity in the pore space. The electrical resistivity of the liquid water

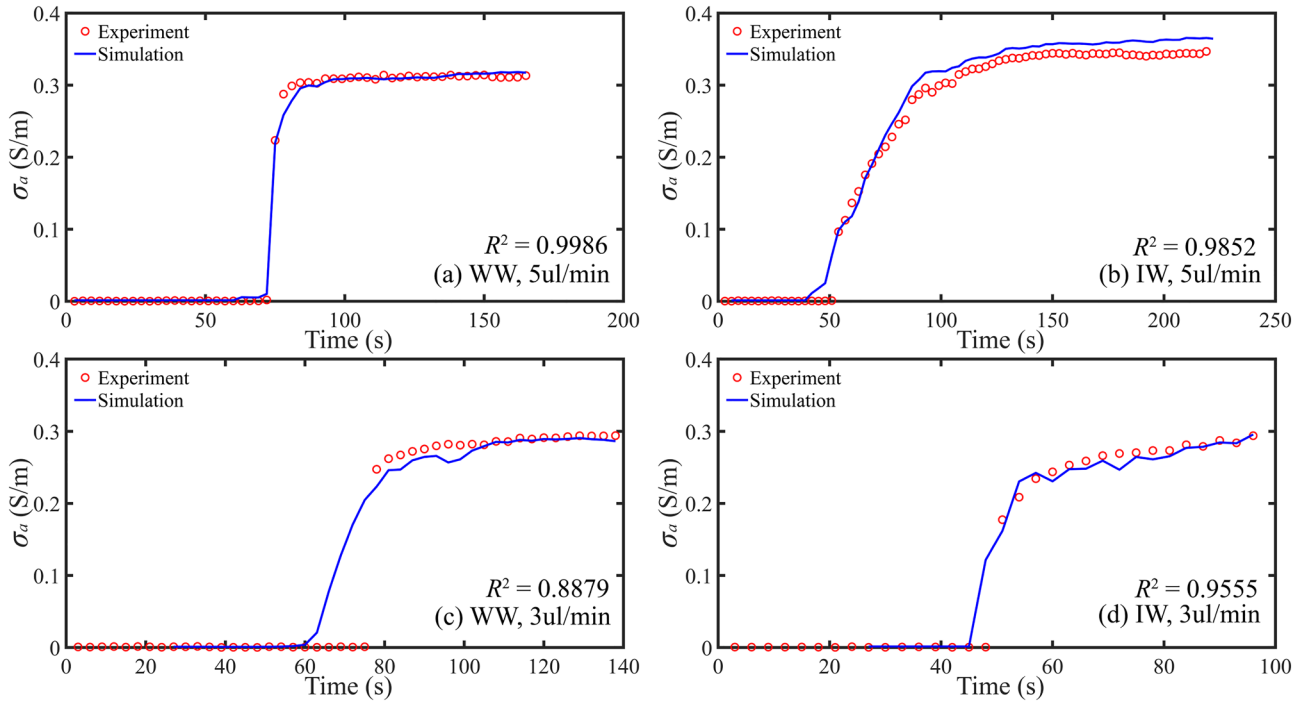

Figure 6. Measured (circles) and simulated (lines) apparent electrical conductivity series for (a) water-wet (WW) micromodel with a water injection rate of 5 μl/min, (b) intermediate-wet (IW) micromodel with a water injection rate of 5 μl/min, (c) WW micromodel with a water injection rate of 3 μl/min, (d) IW micromodel with a water injection rate of 3 μl/min. R^2 measures the goodness of fit between the measured and simulated conductivity.

phase was set to 0.76 S/m, same as the conductivity of the pore water used in the laboratory experiments. The NAPL phase was assigned to 10^{-6} S/m (Jougnot et al., 2018) to avoid significant electrical current entering into the grains. A current flow of 1 mA was used between the electrodes and their voltage difference was simulated to calculate the bulk resistivity. Figure 5 shows a simulated electrical potential distribution for the corresponding CCD image.

3. Results Under Laboratory-Controlled Conditions

3.1. Electrical Resistivity: Experiment and Simulation Results

We plot the measured and simulated time series electrical resistivity of four experiments with different wetting conditions and water injection rates in Figure 6. The y-axis is shown in the form of apparent conductivity $\sigma_a = 1/\rho_a$. The apparent resistivity ρ_a was calculated by $\rho_a = K \times V/I$, where V is the electric voltage between the inlet and outlet faces of the micromodel and I is the measured current. $K = 2.1 \times 10^{-5} m$ denotes the geometric factor and was calculated by COMSOL using the method proposed by Jougnot et al. (2010).

The simulated electrical conductivity agrees well with the measured value in all data series ($R^2 > 0.88$). The discrepancies are mainly contributed by the measurements at time steps close to the threshold when the conductivity starts to increase; the experiment fails to capture the breakthrough of electrical current because the electrodes are still covered completely by the non-conductive NAPL. Nevertheless, we did not consider those deviated data in the following analysis because only experimental data after the breakthrough of conductivity were used.

Figure 7 displays the measured "resistivity index" (where the effect of surface conductivity is not considered) against pore water saturation for the

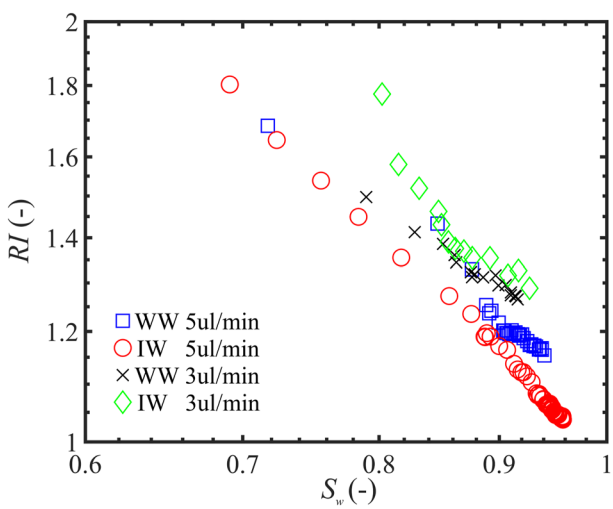

Figure 7. Measured resistivity index as a function of water saturation S_w for water-wet and intermediate-wet conditions with different water injection rates. Note that the effect of surface conductivity is not considered here so the results should be classically fitted by a power-law function.

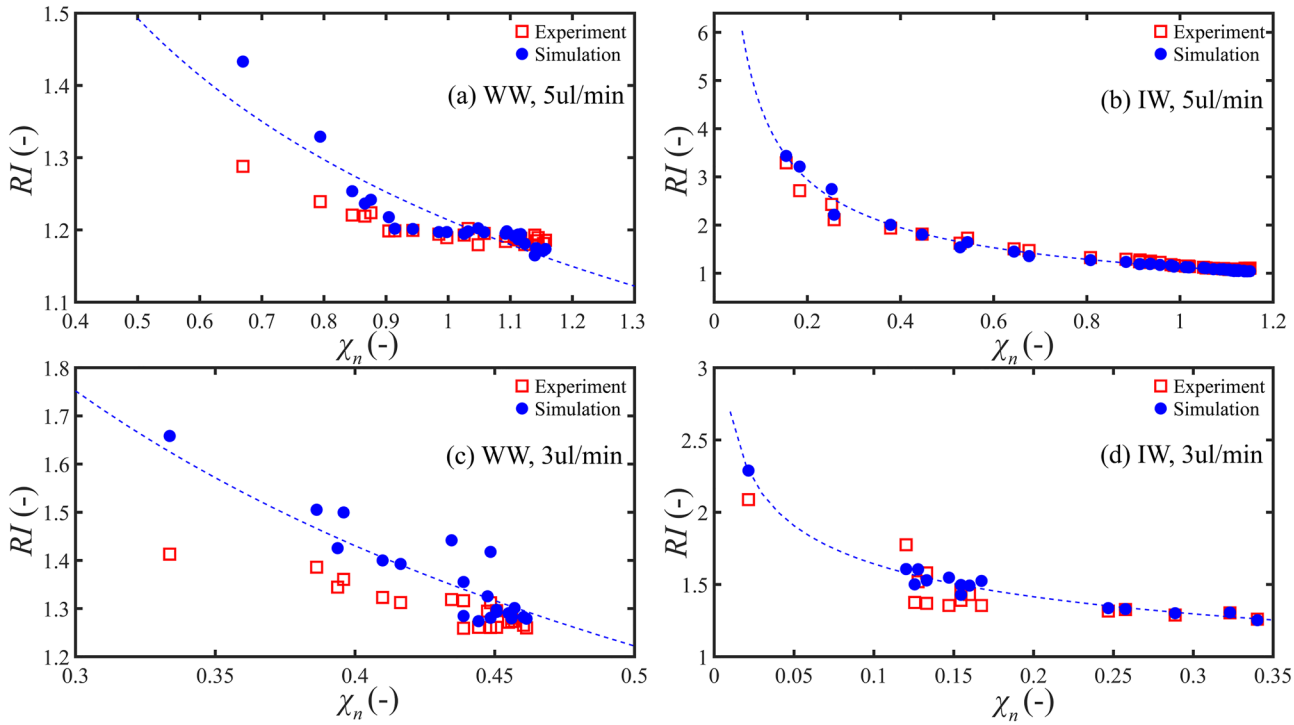

Figure 8. Measured resistivity index as a function of normalized Euler characteristic χ_n for (a) water-wet (WW) micromodel with a water injection rate of 5 µl/min, (b) intermediate-wet (IW) micromodel with a water injection rate of 5 µl/min, (c) WW micromodel with a water injection rate of 3 µl/min, (d) IW micromodel with a water injection rate of 3 µl/min. (where the effect of surface conductivity is not considered).

experiments in Figure 7. The pore water saturation we plot is above 0.6 because the concerned residual behavior of NAPL usually occurs at this water saturation range (Payatakes, 1982) and our experimental data acquired at lower pore saturation tends to be extremely large due to the wide distribution of the non-conductive NAPL phase in the micromodel. The resistivity index shows a clear divergence with different wettability and injection conditions, especially at lower saturation. This indicates a significant impact of NAPL (or water) morphology on the resistivity index. In other words, a single value of Archie's saturation exponent n cannot characterize the resistivity of the porous media with different wettabilities or water injection rates.

3.2. Relationship Between Bulk Resistivity and Normalized Euler Characteristic

In Figure 8, we plot the measured and simulated resistivity index against normalized Euler characteristic of water for the four experiments in Figure 6, the normalized Euler characteristic (χ_n) can be obtained by

$$\chi_n = \frac{1 - \chi_0}{N} \tag{6}$$

where χ_0 is the Euler characteristic of water in the CCD images measured by MATLAB function "regionprops." The relationship between the normalized Euler characteristic and resistivity index (Scholz et al., 2012) can be written according to the "morphology-based" model as:

$$RI = a{\chi_n}^{-\beta} \tag{7}$$

where a is a proportionality constant and β is a power-law exponent. Equation 7 has the same form as Equation 5, but such a reformulation can make the comparison between Equation 7 and Equation 3 ($RI = {S_w}^{-n}$) more intuitive as they share a similar structure.

All experimental and simulated resistivity indices in Figure 8 are correlated with the normalized Euler characteristic. Data in the IW condition shows a more standard power-law relationship than in the WW conditions, indicating that β is larger and the resistivity index is more sensitive to χ_n in the IW conditions. While in the WW

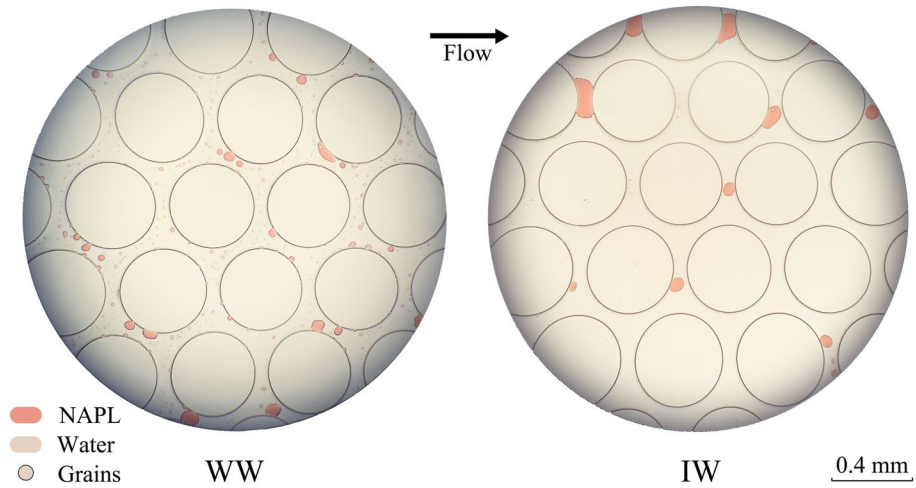

Figure 9. Pore-scale images taken by microscope to illustrate non-aqueous phase liquid ganglia after displacement for water-wet and intermediate-wet conditions with a water injection rate of 5 μl/min. The electric field is applied in the flow direction.

condition the resistivity index curve tends to level off and result in a more linear relationship between χ_n and resistivity index. Figure 9 taken by the microscope shows the morphology of residual NAPL after displacement with a water injection rate of 5 μl/min. The entire pore space of the WW micromodel is occupied by a mass of tiny NAPL ganglia after displacement. NAPL ganglia trapped in the IW micromodel are much less but bigger, which mainly exist in the pore throat normal to the flow direction (Tzimas et al., 1997). The pore water in the WW condition is highly connected due to the small size of NAPL ganglia regardless of NAPL amounts, which results in a relatively larger χ_n of the WW micromodel in Figure 8.

4. Pore Network Modeling Under Uncontrolled Conditions

As shown in the previous section, pore network simulation has proved its effectiveness in evaluating the effects of NAPL morphology on electrical properties under controlled conditions. For the simplified and ideal NAPL distribution conditions (i.e., illustrated in Figures 1 and 2), we constructed two schemes to simulate the electrical resistivity since it is impossible to reproduce the ideal NAPL distribution in the micromodel experiments.

4.1. Simulation Schemes

4.1.1. Scheme 1: Simulation of Residual NAPL With Different Sizes at Specific Positions

Simulation scheme 1 was constructed to explore the effect of the residual NAPL position on bulk resistivity, it simulated all four types of residual NAPL ganglia positions in the pore space using the patchy saturation model (Mustofa et al., 2022; Toms et al., 2006). The pore network was first assumed to be filled with water. NAPL ganglia were then added to the pore network at the positions shown in Figure 1: (a) the parallel pore throat of the flow direction (Figure 1a), (b) the perpendicular pore throat of the flow direction (Figure 1b), (c) the pore center (Figure 1c), (d) rounded rectangular NAPL ganglia form a continuous phase through several pores (Figure 1d). Meanwhile, to evaluate the influence of water saturation on bulk resistivity with different NAPL positions, we simulated a series of water saturation for each specific position, which was implemented by changing the size of the NAPL ganglia: (a) for circular NAPL ganglia (Figures 1a–1c), the diameter of each NAPL ganglia l_g increased from 0 to all the pores were filled, (b) for the continuous rounded rectangular NAPL ganglia (Figure 1d), the width was constant and the length (in the flow direction) increased from 0 to 2 mm. Thus, we can calculate the electrical resistivity of the micromodel with different sizes at specific positions using COMSOL.

4.1.2. Scheme 2: Simulation of Residual NAPL With Specific Size at Different Positions

Simulation scheme 2 was constructed to explore the specific factors that determine β in the morphology-based model and Archie's saturation exponent n in Equation 3. Like scheme 1, the pore network was first assumed to be filled with water. Then, rather than adding circular NAPL in a specific position, we added random amounts

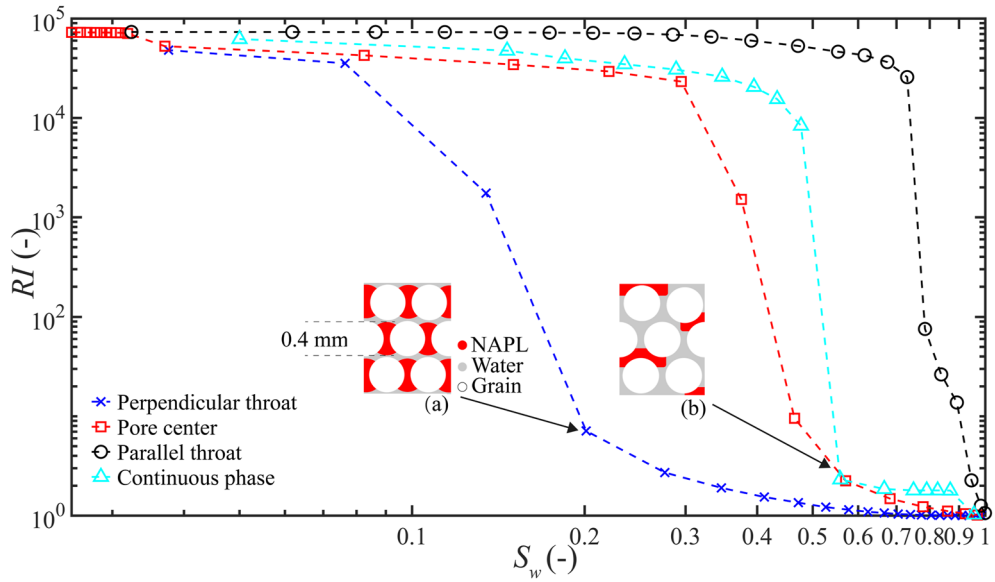

Figure 10. Simulated resistivity index versus water saturation with different residual distributions of non-aqueous phase liquid (NAPL) ganglia in Figure 1: parallel to the flow direction (black circle), perpendicular to the flow direction (blue cross), in the pore center (red square), as a continuous phase through several pores (cyan triangle). The saturation variation is implemented by changing the NAPL ganglia size. Inset: (a) the pore-scale sketch of NAPL ganglia when the diameter l_g of NAPL ganglia equals the diameter of the grains (0.4 mm), (b) the pore-scale sketch of NAPL ganglia when the continuous NAPL phase does not completely block the adjacent pore throat.

(1–2,000) of fixed-size circular NAPL ganglia to the pore space randomly, in this process, some of the NAPL ganglia could be partly covered by the grains and some could overlap with each other and merge into a larger ganglion. We performed 100 simulations for each NAPL ganglia size (from 0.005 to 0.01 mm). The acquired χ_n and S_w were used to fit β and n, respectively.

4.2. Simulation Results

4.2.1. Relationship Between Residual NAPL Ganglia Positions and Bulk Resistivity

Figure 10 plots the simulated resistivity index versus water saturation using simulation scheme 1. The "parallel throat" pattern shows a dramatic variation at high water saturation, indicating a significant effect of NAPL on bulk resistivity. In contrast, those NAPL trapped in a perpendicular throat make nearly no contributions to bulk resistivity until the diameter of NAPL ganglia l_g exceeds the diameter of grains (0.4 mm), which is when they occupy the parallel throat (Figure 10 inset a). Nearly all resistivity index curves show a percolation behavior, for example, the resistivity index of the continuous NAPL phase pattern experiences a sharp decrease when the adjacent pore throat is not completely blocked (Figure 10 inset b), while the resistivity index is almost constant at water saturations out of this range.

4.2.2. Relationship Between Residual NAPL Ganglia Size and the Morphology-Based Model

Using simulation scheme 2, the fitted β in the morphology model (Equation 7) is plotted as a function of estimated average NAPL ganglia diameters $\overline{l_g}$ in Figure 11. The average diameter of NAPL ganglia $\overline{l_g}$ are calculated from all ganglia in a micromodel image. For each NAPL ganglia, the diameter is estimated by the mean of its major and minor axis length. $\overline{l_g}$ has a more extensive range (0.0019–0.0172 mm) than the specified diameters (0.005–0.01 mm) due to the block and overlap of NAPL ganglia in patchy saturation models.

Figure 11 shows that the simulated β has approximately three stages: at the initial stage, $\overline{l_g}$ is smaller than the minimum pore throat width $l_p = 0.07$ mm. β is close to zero and decreases when $\overline{l_g}$ approaches l_p. The typical fitting curve of the resistivity index at this stage is shown in Figure 11a, the resistivity index increases with χ_n in a minimal range. Then, β changes dramatically at a critical stage when the 95% upper confidence limit of $\overline{l_g}$ close

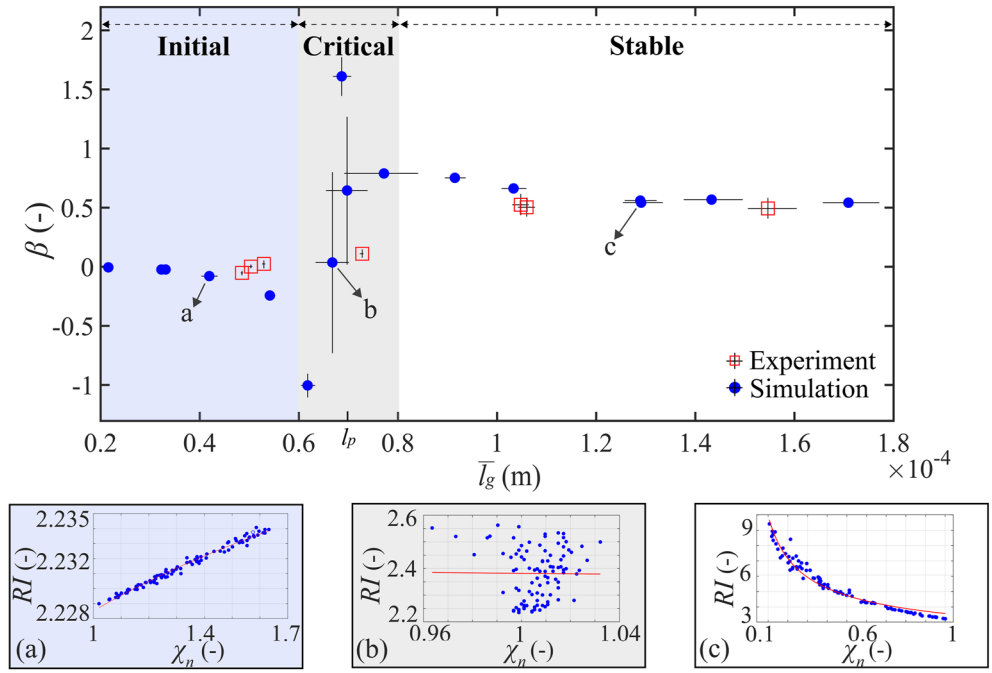

Figure 11. Fitted β of simulated (blue circle) and measured data (red square) against the estimated average size of residual non-aqueous phase liquid (NAPL) ganglia $\overline{l_g}$. The solid black line on data points indicates the 95% confidence interval of β (vertical line) and estimated NAPL ganglia diameter (horizontal line). l_p on the x-axis equals the minimum pore throat width 0.07 mm of the micromodel. Inset: curves of simulated resistivity index versus normalized Euler characteristic for corresponding data points at (a) initial stage, (b) critical stage, (c) stable stage in the main figure.

to l_p, and the confidence interval of fitted β also becomes very large, indicating that there is nearly no correlation between the resistivity and χ_n (Figure 11b). Finally, when $\overline{l_g}$ exceeds l_p, β stays at around 0.56 and the bulk resistivity obey a typical power-law relationship with χ_n (Figure 11c). In summary, the fitted β can be regarded as a power scaling of the average NAPL ganglia size with an asymptote at $\overline{l_g} \approx l_p$.

We also plot a series of β fitted by experiment data in Figure 11, which is acquired from the WW and IW micromodels with an injection rate of 5 and 3 μl/min. As $\overline{l_g}$ changes dramatically during the early stage of the displacement, only the χ_n and resistivity index at when the $\overline{l_g}$ is stable are selected to fit β. The experiment data successfully captures the behavior of exponent β at the first and third stages. However, it misses the critical behavior at the second stage, especially the curve fluctuation near the pore throat width l_p. This is because the NAPL phase images obtained from experiments are a mixture of different NAPL patterns, that is, all four situations in Figure 2 can exist simultaneously in a single image. Hence the critical behavior caused by a specific pattern (Figure 2c) is diminished. Besides, the neglection of NAPL ganglia that are smaller than the pixel size of the CCD image (8 μm) or incorrectly identified tiny NAPL clusters as noises can make the image lose some detail (Latief et al., 2017; Yang et al., 2021). These resolution errors are not an issue when there are no tiny crevices and corners in a homogeneous cylindrical media (Liu et al., 2017), but it influences the calculation of χ_n because the restoration of the non-conductive phase connectivity is highly dependent on image resolution. These resolution errors also cause inconsistencies between the real NAPL distribution and the COMSOL interpolation function in the numerical modeling, which may lead to the scattering of simulation results in Figure 6.

Another inconsistency between experiments and simulations is that the absolute value of exponent β is relatively small in the experiments. This is likely because all experimental χ_n and resistivity index values used to fit the curve were chosen with water saturation higher than the residual water saturation while the power scaling of the resistivity index to χ_n is expected to occur only in the vicinity of the percolation threshold itself (Liu et al., 2018; Scholz et al., 2012, 2015). A complete displacement data series would have a much larger exponent β because the NAPL ganglia size increases dramatically with NAPL saturation. This conclusion is also true for the simulated

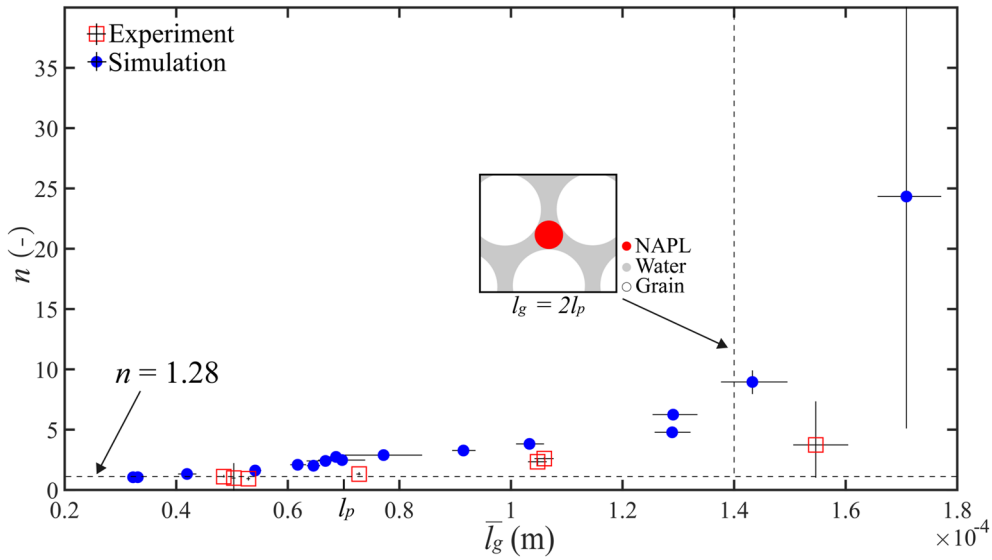

Figure 12. Fitted Archie's saturation exponent n of simulated (blue circle) and measured data (red square) versus estimated average size of residual non-aqueous phase liquid (NAPL) ganglia $\overline{l_g}$. The solid black line on data points indicates the 95% confidence interval of β (vertical line) and NAPL ganglia diameter (horizontal line). Inset: pore-scale sketch of the residual NAPL morphology when the NAPL ganglia happen to be at the pore center and the diameter $l_g = 2\,l_p$ (0.14 mm).

results at high water saturations as the relationship between resistivity index and χ_n at stable stage (Figure 11 inset c) is more of a linear correlation rather than power-law.

4.2.3. Relationship Between Residual NAPL Ganglia Size and the Archie's Saturation Exponent

In Figure 12, we plot the fitted values of the Archie's saturation exponent n versus the average size of the residual NAPL ganglia in the pore space using simulation scheme 2 as in the morphology-based model. Nearly all the fitted values of n characterized by small NAPL sizes have a narrow confidence interval. In turn, this indicates a typical power-law relationship between the resistivity index and saturation. An increase in the estimated NAPL ganglia diameter from 0 to 2 l_p (Figure 12) only results in a small increase of n. On the opposite, a slight increase in NAPL size larger than 2 l_p leads to a dramatic change in the value of n. The R^2-coefficient between the simulated n and an optimal power-law fitting is 0.9283, indicating a power-law behavior between n and $\overline{l_g}$. We also plot the n acquired from the experiments (Figure 12). Deviations between the experiment and simulation results may also be caused by the data loss near the percolation thresholds (Scholz et al., 2015).

5. Discussions

5.1. Effect of Surface Conduction on the Micromodel Resistivity

Surface conduction is assumed to be absent in this work, which is considered reasonable because the micromodel is made of pure silica with a low specific surface area, which has lower surface conductivity than those clayey porous media (Jougnot et al., 2018; Revil et al., 2017). However, the results could not demonstrate that the surface conduction in our micromodel is negligible. Further elaborate discussions on the surface conductivity in porous media are required. In presence of surface conduction, IP provides a quantity named normalized chargeability that can be used to estimate surface conductivity (Niu et al., 2016; Revil, 2012). Nevertheless, the observed relationships between the resulting β in Figure 11, n in Figure 12 and the NAPL ganglia size would be valid whether surface conductivity is present or not.

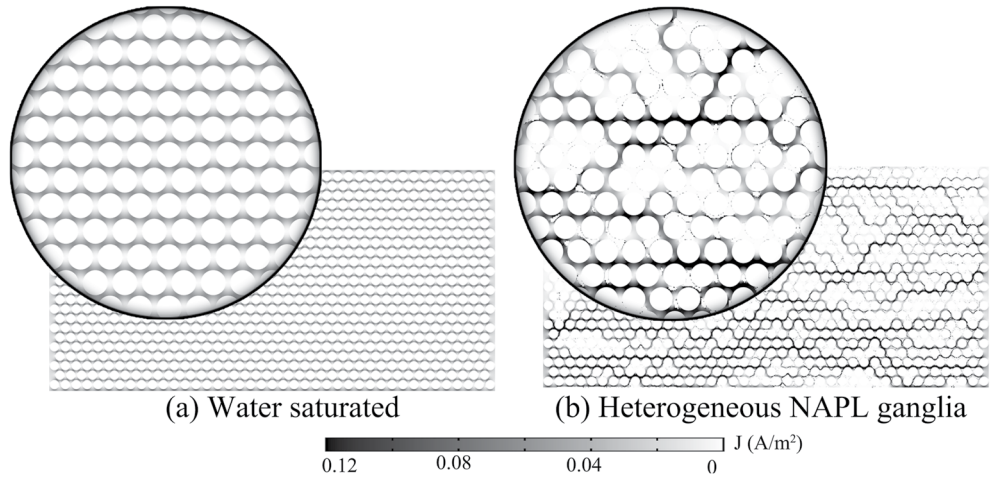

Figure 13. The current density distribution when (a) heterogeneous non-aqueous phase liquid (NAPL) ganglia block the pore space and (b) the pore space is saturated with water. There is a significant change in the tortuosity of the current pathways in the presence of the NAPL ganglia.

5.2. Effect of Residual NAPL Positions on Electrical Resistivity

We discuss now the relationship between the residual NAPL ganglia position and the bulk resistivity. The residual NAPL phase morphology during displacement is directly controlled by capillary number (Lenormand et al., 1988), which is given by

$$C_a = \frac{Q_w \mu_w}{W D \gamma} \tag{8}$$

where Q_w is the injection rate, μ_w is water viscosity, W and D are the width and the etching depth of the pore channel, respectively. γ is the water-NAPL interfacial tension, which is associated with wettability. As shown in Figure 9, for the WW conditions, the snap-off of NAPL is favored during displacements since NAPL tends to break and be trapped due to the pressure difference across the water-NAPL interface (Payatakes, 1982). For the IW condition, the contact angle of water to the pore network increase and the snap-off of NAPL is favored less. In this case, the piston-like filling dominates the displacement (Yang et al., 2007), hence there are only a few NAPL ganglia stay in the pore throats that parallel to the main flow direction. At the same time, NAPL in the perpendicular pore throats is harder to be washed out because of the increased contact angle of water to the pore channel.

The simulated results in Figure 10 suggest that the bulk resistivity of porous media can be intuitively related to the degree of congestion in the pore space. While different positions of the congestion may play a different role in the bulk resistivity according to their impact on the pore water connectivity. None of the simulation results in Figure 10 follow a linear relationship in the log scale axis (i.e., the Archie's second law). This deviation is because Archie's second law assumes all NAPL phase in the pore space equivalently contributes to the electrical resistivity (Grattoni & Dawe, 1995). This assumption is reasonable for most conditions in porous media when NAPL phases are distributed randomly in the pore space. However, once the NAPL phase regularly distributes at different positions of the pore space that contributed differently to the bulk resistivity, such as in simulation scheme 1, the Archie's second law would not be applicable.

In Figure 13, we simulate the current density distribution at fully (Figure 13a) and partially (Figure 13b) water-saturated conditions. In the former case, the current flow mainly through the pore channels that parallel to the flow direction, the perpendicular pore throats then play a role as temporary “dead ends” (Coats & Smith, 1964) for the current flow. This current density distribution explains why at high saturation in Figure 7, the WW micromodel with a displacement rate of 5 μl/min has higher resistivity than the IW micromodel: most of the NAPL ganglia in the IW conditions are trapped in perpendicular pore throats with small current density (Figure 9). According to Ohm's law ($V = I \times R$), if the electric current I flow through a pore throat equals zero, the electrical voltage difference V between the two sides of the pore throat would also equal to zero regardless of

the resistance inside the pore throats. This indicates that the saturation of NAPL phase at the dead end pore throat would not affect the electric voltage field, and therefore not contribute to the bulk resistivity. Revil et al. (2018) observed a similar phenomenon in a 3D pore geometry, which is a key point for the deviations in resistivity from the Archie's second law for macroscale processes. Porous media may show different bulk resistivity at same water saturation due to different NAPL morphologies in the pore space.

Nevertheless, as we mentioned before, for most porous media, the NAPL phase can not be retained at a specific position of the pore space (such as that shown in Figure 1). When NAPL blocks the parallel pore throats in our micromodel, the current path will switch to the perpendicular pore throats (Figure 13b) that are not blocked by the NAPL ganglia. Then the original dead end (perpendicular pore throats) will become the current path, and some of the parallel pore throats become the new dead-end area. Thus, the difference in the NAPL ganglia position is not enough to account for the resistivity difference in Figure 7. Because even in the IW conditions, there are still NAPL ganglia that block the parallel pore throat at a small injection rate. Therefore, the comprehensive morphology-based model that considers more sufficient properties of the residual NAPL, such as the amount, size, and position of the NAPL ganglia, should be further introduced to analyze the relationship between NAPL morphology and bulk resistivity quantitatively.

5.3. Effect of Residual NAPL Ganglia Size on the Morphology-Based Model

Scholz et al. (2015) suggested that β in the morphology-based model (Equation 7) is equal to the cementation exponent m in the Archie's first law for randomly overlapping monodisperse circles and ellipses structures. However, Liu et al. (2018) acquired a value range from -0.72 to 1 for β in 3D two-phase flow simulations by changing the wettability and displacement rates. Mustofa et al. (2022) indicated that there is no specific relationship between χ_n and resistivity index in some specific wettability models by micro-CT and column experiments. In addition, although both our experimental and numerical results in IW conditions reveal a correlation between the resistivity index and χ_n (Figure 8), the resistivity index in WW conditions tends to linearly depend on χ_n rather than power scaling. These results suggest that β is not constant for a specific pore structure at partial saturation. It is associated with the morphology of residual NAPL in the pore space, which is determined by the wettability and displacement rate (capillary number).

Scholz et al. (2015) interpreted Euler characteristics in water-saturated systems as the density of the current pathway obstacles formed by joined individual grains. A similar theory can be extended to the partially saturated systems, where the current pathway obstacles are formed by grains and NAPL ganglia. Thus, the three stages of β in Figure 11 can be related to different spatial patterns of residual NAPL ganglia in the pore space (see Figure 2). When l_g is small at the initial stage of β, NAPL ganglia exist as tiny particles as shown in Figure 2b. These particles could reduce the Euler characteristic of water but do not affect the bulk resistivity significantly due to their small size. Therefore, the resistivity index increased slowly with the Euler characteristic at this stage, resulting in a β close to 0. When l_g approaches l_p, the effect of NAPL ganglia on bulk resistivity become notable and β decreased accordingly. For l_g at the critical stage, (i.e., $l_g \approx l_p$), most of the NAPL ganglia exist in the pattern of Figure 2c. The NAPL ganglia are large enough to block the pore throat and affect bulk resistivity, but the NAPL ganglia cannot connect adjacent grains on a large scale. The Euler characteristic at this time stays the same as the case in which the pore space is fully saturated with water (Figure 2a). As a result, the resistivity index and Euler characteristic are no longer relevant in the "critical zone" (see Figure 11). Then, l_g keeps increase until $l_g > l_p$ (Figure 2d). At this stage, the NAPL ganglia can easily contact with more than one grain and form non-conductive "bridges" between the grains. The Euler characteristic rises as the number of independent closed non-conductive phases decreases. Hence, the resistivity index and Euler characteristic in the $l_g > l_p$ case are both susceptible to the amount of the NAPL ganglia, leading to a stable and considerable value of β.

In summary, both the simulation and experimental results in Figure 11 suggest that the exponent β in the morphology-based model depends on the size of NAPL ganglia. This may explain the various values taken by the exponent β observed under different wetting conditions (Liu et al., 2018; Mustofa et al., 2022; Scholz et al., 2015).

5.4. Effect of Residual NAPL Ganglia Size on the Archie's Saturation Exponent

Although the morphology-based model can intuitively reveal the relationship between electrical resistivity and NAPL morphology, it is difficult to measure the Euler characteristic of natural porous media, especially for 3D structures. Therefore, the Archie's second law is still a widely applied model as it focuses on an easy-to-measure characteristic, water saturation. In general, the Archie's saturation exponent n and the exponent μ in percolation theory represent the same mechanism: account for the reduction in connectivity of the water (Binley & Slater, 2020; Tercier, 1992). In previous works, a value range from 1 to 1.5 or fixed 1.28 were usually observed for μ in 2D pore networks (Derrida & Vannimenus, 1982; Kozlov et al., 2012; Sahimi, 1984). Indeed, our simulated and measured n in Figure 12 are also close to these values at NAPL ganglia size $\overline{l_g} < l_p$, which is usually the largest size for residual NAPL ganglia in the WW conditions because the larger ganglia are likely to snap off and become as big as or smaller than the pore throat. Thus, the asymptotic value of the Archie's saturation exponent n (~1.28) seems to be a rough estimate for various WW porous media. Han et al. (2021) came to a similar conclusion in 3D structures. In their work, another morphology parameter of the non-conductive phase, aspect ratio, was discussed for its influence on the Archie's saturation exponent.

Ellis et al. (2010) demonstrated that the bulk contribution of the electrical resistivity of porous media is proportional to the path length taken by the mobile charge carriers, which are distributed preferentially in different fluid phases. Glover (2017) then interpreted the Archie's saturation exponent n as the qualitative measure of the water connectivity change rate with saturation. This conclusion is supported by our results that the Archie's saturation exponent n begins to increase dramatically when $\overline{l_g}$ exceeds $2\,l_p$. The diameter $l_g = 2\,l_p$ for NAPL ganglia can result in a particular case: the NAPL ganglia equal the largest hard-sphere that can be placed in the pore center (inset of Figure 12). As an ideal case, it could provide an epitome of NAPL morphology when the NAPL ganglia size is relatively large. In this case, n increases extremely fast because when the NAPL ganglia get larger. Both the parallel and perpendicular pore throats can be clogged entirely. A slight increase in NAPL ganglia size (NAPL saturation) may cause a considerable reduction in water connectivity. These results indicate that n is highly depends on the size of residual NAPL ganglia, and can be interpreted as the rate of change of charge carrier path connectivity to water saturation. The change of n with water saturation and wettablities in some porous media (Abdassah et al., 1998; Glover, 2017; Montaron, 2009) can be explained by the variation in NAPL ganglia size.

6. Conclusions

We measured the resistivity of 2D-micromodels with different spatial patterns of NAPL morphology at pore-scale. The results show that the bulk resistivity of porous media relies highly on the residual NAPL distribution. NAPL distributed in dead ends of the pore space has little impact on the bulk resistivity because they do not control the current path and the voltage distribution.

The correlations between the resistivity index of the partially saturated porous media and the normalized Euler characteristic of water phase change with the relative size of residual NAPL ganglia to the pore throats. A typical power-law relationship between bulk resistivity and normalized Euler characteristic of the water phase can be established when the NAPL ganglia are large enough to block the pore throats completely.

The NAPL ganglia size influences the Archie's saturation exponent. A power-law relationship is found between the Archie's saturation exponent n and the average size of residual NAPL ganglia, which suggests that n can be interpreted as the rate of change of the pore water connectivity with saturation. These insights provide a more physical interpretation of the Archie's second law. Future studies should extend these relationships to 3D structures, as well as incorporate the effect of NAPL phase morphology and wettability on surface conductivity and IP.

Data Availability Statement

The experimental & synthetic raw data and sample MATLAB codes used for image process and analysis in this study are available at this site (https://doi.org/10.5281/zenodo.6809646).

Acknowledgments
The work was supported by the National Natural Science Foundation of China (41977157, 42272276). We are grateful to Editor Kamini Singha, Associate Editor Andrew Binley, and three anonymous reviewers for their insightful comments and suggestions, which significantly improve the quality of this work. We also would like to thank Tengfei Ma at Nanjing University for his support in designing the micromodel.

References

Abdassah, D., Permadi, P., Sumantri, Y., & Sumantri, R. (1998). Saturation exponent at various wetting condition: Fractal modeling of thin-sections. *Journal of Petroleum Science and Engineering*, *20*(3–4), 147–154. https://doi.org/10.1016/S0920-4105(98)00014-X

Al-Raoush, R. I. (2009). Impact of wettability on pore-scale characteristics of residual nonaqueous phase liquids. *Environmental Science & Technology*, *43*(13), 4796–4801. https://doi.org/10.1021/es802566s

Archie, G. E. (1942). The electrical resistivity log as an aid in determining some reservoir characteristics. *Transactions of the AIME*, *146*(01), 54–62. https://doi.org/10.2118/942054-G

Armstrong, R. T., McClure, J. E., Robins, V., Liu, Z., Arns, C. H., Schlüter, S., & Berg, S. (2019). Porous media characterization using Minkowski functionals: Theories, applications and future directions. *Transport in Porous Media*, *130*(1), 305–335. https://doi.org/10.1007/s11242-018-1201-4

Binley, A., & Kemna, A. (2005). DC resistivity and induced polarization methods. In Y. Rubin & S. S. Hubbard (Eds.), *Hydrogeophysics* (pp. 129–156). Springer. https://doi.org/10.1007/1-4020-3102-5_5

Binley, A., & Slater, L. (2020). *Resistivity and induced polarization: Theory and applications to the near-surface earth*. Cambridge University Press.

Bruggeman, V. D. (1935). Berechnung verschiedener physikalischer Konstanten von heterogenen Substanzen. I. Dielektrizitätskonstanten und Leitfähigkeiten der Mischkörper aus isotropen Substanzen. *Annalen der Physik*, *416*(7), 636–664. https://doi.org/10.1002/andp.19354160705

Bücker, M., Orozco, A. F., Hördt, A., & Kemna, A. (2017). An analytical membrane-polarization model to predict the complex conductivity signature of immiscible liquid hydrocarbon contaminants. *Near Surface Geophysics*, *15*(6), 547–562. https://doi.org/10.3997/1873-0604.2017051

Coats, K., & Smith, B. (1964). Dead-end pore volume and dispersion in porous media. *Society of Petroleum Engineers Journal*, *4*(01), 73–84. https://doi.org/10.2118/647-PA

Cosenza, P., Ghorbani, A., Camerlynck, C., Rejiba, F., Guérin, R., & Tabbagh, A. (2009). Effective medium theories for modelling the relationships between electromagnetic properties and hydrological variables in geomaterials: A review. *Near Surface Geophysics*, *7*(5–6), 563–578. https://doi.org/10.3997/1873-0604.2009009

Daily, W., Ramirez, A., LaBrecque, D., & Barber, W. (1995). Electrical resistance tomography experiments at the Oregon Graduate Institute. *Journal of Applied Geophysics*, *33*(4), 227–237. https://doi.org/10.1016/0926-9851(95)90043-8

Dekker, T. J., & Abriola, L. M. (2000). The influence of field-scale heterogeneity on the surfactant-enhanced remediation of entrapped nonaqueous phase liquids. *Journal of Contaminant Hydrology*, *42*(2–4), 219–251. https://doi.org/10.1016/S0169-7722(99)00091-1

Deng, Y., Shi, X., Revil, A., Wu, J., & Ghorbani, A. (2018). Complex conductivity of oil-contaminated clayey soils. *Journal of Hydrology*, *561*, 930–942. https://doi.org/10.1016/j.jhydrol.2018.04.055

Deng, Y., Shi, X., Xu, H., Sun, Y., Wu, J., & Revil, A. (2017). Quantitative assessment of electrical resistivity tomography for monitoring DNAPLs migration–Comparison with high-resolution light transmission visualization in laboratory sandbox. *Journal of Hydrology*, *544*, 254–266. https://doi.org/10.1016/j.jhydrol.2016.11.036

Derrida, B., & Vannimenus, J. (1982). A transfer-matrix approach to random resistor networks. *Journal of Physics A: Mathematical and General*, *15*(10), L557–L564. https://doi.org/10.1088/0305-4470/15/10/007

Du, Y., Mehmani, A., Xu, K., Kelly, S., Balhoff, M., & Torres-Verdín, C. (2020). Microfluidic diagnostics of the impact of local microfracture connectivity on hydrocarbon recovery following water injection. *Water Resources Research*, *56*(7), e2019WR026944. https://doi.org/10.1029/2019WR026944

Dwarakanath, V., Jackson, R. E., & Pope, G. A. (2002). Influence of wettability on the recovery of NAPLs from alluvium. *Environmental Science & Technology*, *36*(2), 227–231. https://doi.org/10.1021/es011023w

Ellis, M. H., Sinha, M. C., Minshull, T. A., Sothcott, J., & Best, A. I. (2010). An anisotropic model for the electrical resistivity of two-phase geologic materials. *Geophysics*, *75*(6), E161–E170. https://doi.org/10.1190/1.3483875

Glover, P. W. (2017). A new theoretical interpretation of Archie's saturation exponent. *Solid Earth*, *8*(4), 805–816. https://doi.org/10.5194/se-8-805-2017

Grattoni, C. A., & Dawe, R. A. (1995). Influence of fluid distribution upon electrical resistivity of partially saturated media. In *Paper presented at the SPWLA 36th annual logging symposium*.

Han, T.-C., Yan, H., & Fu, L.-Y. (2021). A quantitative interpretation of the saturation exponent in Archie's equations. *Petroleum Science*, *18*(2), 444–449. https://doi.org/10.1007/s12182-021-00547-0

Higham, D. J., & Higham, N. J. (2016). *MATLAB guide* (3rd ed.). Society for Industrial and Applied Mathematics. https://doi.org/10.1137/1.9781611974669

Izumoto, S., Huisman, J. A., Zimmermann, E., Heyman, J., Gomez, F., Tabuteau, H., et al. (2022). Pore-scale mechanisms for spectral induced polarization of calcite precipitation inferred from geo-electrical millifluidics. *Environmental Science & Technology*, *56*(8), 4998–5008. https://doi.org/10.1021/acs.est.1c07742

Jing, Y., Armstrong, R. T., Ramandi, H. L., & Mostaghimi, P. (2017). Topological characterization of fractured coal. *Journal of Geophysical Research: Solid Earth*, *122*(12), 9849–9861. https://doi.org/10.1002/2017JB014667

Johansson, S., Fiandaca, G., & Dahlin, T. (2015). Influence of non-aqueous phase liquid configuration on induced polarization parameters: Conceptual models applied to a time-domain field case study. *Journal of Applied Geophysics*, *123*, 295–309. https://doi.org/10.1016/j.jappgeo.2015.08.010

Jougnot, D., Ghorbani, A., Revil, A., Leroy, P., & Cosenza, P. (2010). Spectral induced polarization of partially saturated clay-rocks: A mechanistic approach. *Geophysical Journal International*, *180*(1), 210–224. https://doi.org/10.1111/j.1365-246X.2009.04426.x

Jougnot, D., Jiménez-Martínez, J., Legendre, R., Le Borgne, T., Méheust, Y., & Linde, N. (2018). Impact of small-scale saline tracer heterogeneity on electrical resistivity monitoring in fully and partially saturated porous media: Insights from geoelectrical milli-fluidic experiments. *Advances in Water Resources*, *113*, 295–309. https://doi.org/10.1016/j.advwatres.2018.01.014

Kang, X., Kokkinaki, A., Kitanidis, P. K., Shi, X., Revil, A., Lee, J., et al. (2020). Improved characterization of DNAPL source zones via sequential hydrogeophysical inversion of hydraulic-head, self-potential and partitioning tracer data. *Water Resources Research*, *56*(8), e2020WR027627. https://doi.org/10.1029/2020WR027627

Kang, X., Shi, X., Deng, Y., Revil, A., Xu, H., & Wu, J. (2018). Coupled hydrogeophysical inversion of DNAPL source zone architecture and permeability field in a 3D heterogeneous sandbox by assimilation time-lapse cross-borehole electrical resistivity data via ensemble Kalman filtering. *Journal of Hydrology*, *567*, 149–164. https://doi.org/10.1016/j.jhydrol.2018.10.019

Kovscek, A., Wong, H., & Radke, C. (1993). A pore-level scenario for the development of mixed wettability in oil reservoirs. *AIChE Journal*, *39*(6), 1072–1085. https://doi.org/10.1002/aic.690390616

Kozlov, B., Schneider, M., Montaron, B., Lagues, M., & Tabeling, P. (2012). Archie's law in microsystems. *Transport in Porous Media*, *95*(1), 1–20. https://doi.org/10.1007/s11242-012-0029-6

Lan, T., Hu, R., Guo, W., Wei, G. J., Chen, Y. F., & Zhou, C. B. (2022). Direct prediction of fluid-fluid displacement efficiency in ordered porous media using the pore structure. *Water Resources Research*, *58*(7), e2021WR031875. https://doi.org/10.1029/2021WR031875

Latief, F., Fauzi, U., Irayani, Z., & Dougherty, G. (2017). The effect of X-ray micro computed tomography image resolution on flow properties of porous rocks. *Journal of Microscopy*, *266*(1), 69–88. https://doi.org/10.1111/jmi.12521

Lenormand, R., Touboul, E., & Zarcone, C. (1988). Numerical models and experiments on immiscible displacements in porous media. *Journal of Fluid Mechanics*, *189*, 165–187. https://doi.org/10.1017/S0022112088000953

Lim, J. S. (1990). *Two-dimensional signal and image processing*. Prentice Hall.

Liu, Z., Herring, A., Arns, C., Berg, S., & Armstrong, R. T. (2017). Pore-scale characterization of two-phase flow using integral geometry. *Transport in Porous Media*, *118*(1), 99–117. https://doi.org/10.1007/s11242-017-0849-5

Liu, Z., McClure, J. E., & Armstrong, R. T. (2018). Influence of wettability on phase connectivity and electrical resistivity. *Physical Review E*, *98*(4), 043102. https://doi.org/10.1103/PhysRevE.98.043102

Mecke, K., & Arns, C. (2005). Fluids in porous media: A morphometric approach. *Journal of Physics: Condensed Matter*, *17*(9), S503–S534. https://doi.org/10.1088/0953-8984/17/9/014

Mendieta, A., Jougnot, D., Leroy, P., & Maineult, A. (2021). Spectral induced polarization characterization of non-consolidated clays for varying salinities—An experimental study. *Journal of Geophysical Research: Solid Earth*, *126*(4), e2020JB021125. https://doi.org/10.1029/2020JB021125

Montaron, B. (2009). Connectivity theory–a new approach to modeling non-Archie rocks. *Petrophysics*, *50*(02), 102–115.

Mustofa, M. B., Fauzi, U., Latief, F. D. E., & Warsa, W. (2022). Experimental and modeling of electrical resistivity changes due to micro-spatial distribution of fluid for unconsolidated sand. *Journal of Petroleum Science and Engineering*, *208*, 109472. https://doi.org/10.1016/j.petrol.2021.109472

National Research Council. (2013). *Alternatives for managing the nation's complex contaminated groundwater sites*. National Academies Press.

Newgord, C., Posenato Garcia, A., & Heidari, Z. (2019). A new method to quantify wettability from resistivity measurements: Workflow development and experimental core-scale verification. In *Paper presented at SPE Europec featured at 81st EAGE conference*. https://doi.org/10.2118/195565-MS

Newgord, C., Posenato Garcia, A., & Heidari, Z. (2020). Joint interpretation of electrical resistivity and T2 NMR measurements to estimate wettability and water saturation. *SPE Reservoir Evaluation and Engineering*, *23*(02), 772–782. https://doi.org/10.2118/200499-PA

Niu, Q., Revil, A., & Saidian, M. (2016). Salinity dependence of the complex surface conductivity of the Portland sandstone. *Geophysics*, *81*(2), D125–D140. https://doi.org/10.1190/geo2015-0426.1

Otsu, N. (1979). A threshold selection method from gray-level histograms. *IEEE Transactions on Systems, Man, and Cybernetics*, *9*(1), 62–66. https://doi.org/10.1109/TSMC.1979.4310076

Park, S., Anggraini, T. M., Chung, J., Kang, P. K., & Lee, S. (2021). Microfluidic pore model study of precipitates induced by the pore-scale mixing of an iron sulfate solution with simulated groundwater. *Chemosphere*, *271*, 129857. https://doi.org/10.1016/j.chemosphere.2021.129857

Payatakes, A. (1982). Dynamics of oil ganglia during immiscible displacement in water-wet porous media. *Annual Review of Fluid Mechanics*, *14*(1), 365–393. https://doi.org/10.1146/annurev.fl.14.010182.002053

Power, C., Gerhard, J. I., Tsourlos, P., Soupios, P., Simyrdanis, K., & Karaoulis, M. (2015). Improved time-lapse electrical resistivity tomography monitoring of dense non-aqueous phase liquids with surface-to-horizontal borehole arrays. *Journal of Applied Geophysics*, *112*, 1–13. https://doi.org/10.1016/j.jappgeo.2014.10.022

Rangel-German, E., & Kovscek, A. (2006). A micromodel investigation of two-phase matrix-fracture transfer mechanisms. *Water Resources Research*, *42*(3). https://doi.org/10.1029/2004WR003918

Revil, A. (2012). Spectral induced polarization of shaly sands: Influence of the electrical double layer. *Water Resources Research*, *48*(2), W02517. https://doi.org/10.1029/2011WR011260

Revil, A., Ahmed, A. S., & Matthai, S. (2018). Transport of water and ions in partially water-saturated porous media. Part 3. Electrical conductivity. *Advances in Water Resources*, *121*, 97–111. https://doi.org/10.1016/j.advwatres.2018.08.007

Revil, A., Coperey, A., Shao, Z., Florsch, N., Fabricius, I. L., Deng, Y., et al. (2017). Complex conductivity of soils. *Water Resources Research*, *53*(8), 7121–7147. https://doi.org/10.1002/2017WR020655

Revil, A., & Glover, P. (1998). Nature of surface electrical conductivity in natural sands, sandstones, and clays. *Geophysical Research Letters*, *25*(5), 691–694. https://doi.org/10.1029/98GL00296

Revil, A., Kessouri, P., & Torres-Verdín, C. (2014). Electrical conductivity, induced polarization, and permeability of the Fontainebleau sandstone. *Geophysics*, *79*(5), D301–D318. https://doi.org/10.1190/geo2014-0036.1

Revil, A., Schmutz, M., & Batzle, M. L. (2011). Influence of oil wettability upon spectral induced polarization of oil-bearing sands. *Geophysics*, *76*(5), A31–A36. https://doi.org/10.1190/geo2011-0006.1

Sahimi, M. (1984). On the relationship between the critical exponents of percolation conductivity and static exponents of percolation. *Journal of Physics A: Mathematical and General*, *17*(11), L601–L607. https://doi.org/10.1088/0305-4470/17/11/009

Sahini, M., & Sahimi, M. (1994). *Applications of percolation theory*. CRC Press. https://doi.org/10.1201/9781482272444

Sahloul, N. A., Ioannidis, M. A., & Chatzis, I. (2002). Dissolution of residual non-aqueous phase liquids in porous media: Pore-scale mechanisms and mass transfer rates. *Advances in Water Resources*, *25*(1), 33–49. https://doi.org/10.1016/S0309-1708(01)00025-2

Schmutz, M., Revil, A., Vaudelet, P., Batzle, M., Viñao, P. F., & Werkema, D. (2010). Influence of oil saturation upon spectral induced polarization of oil-bearing sands. *Geophysical Journal International*, *183*(1), 211–224. https://doi.org/10.1111/j.1365-246X.2010.04751.x

Schneider, C. A., Rasband, W. S., & Eliceiri, K. W. (2012). NIH image to ImageJ: 25 years of image analysis. *Nature Methods*, *9*(7), 671–675. https://doi.org/10.1038/nmeth.2089

Scholz, C., Wirner, F., Götz, J., Rüde, U., Schröder-Turk, G. E., Mecke, K., & Bechinger, C. (2012). Permeability of porous materials determined from the Euler characteristic. *Physical Review Letters*, *109*(26), 264504. https://doi.org/10.1103/PhysRevLett.109.264504

Scholz, C., Wirner, F., Klatt, M. A., Hirneise, D., Schröder-Turk, G. E., Mecke, K., & Bechinger, C. (2015). Direct relations between morphology and transport in Boolean models. *Physical Review E*, *92*(4), 043023. https://doi.org/10.1103/PhysRevE.92.043023

Singha, K., & Gorelick, S. M. (2006). Effects of spatially variable resolution on field-scale estimates of tracer concentration from electrical inversions using Archie's law. *Geophysics*, *71*(3), G83–G91. https://doi.org/10.1190/1.2194900

Slater, L., & Binley, A. (2021). Advancing hydrological process understanding from long-term resistivity monitoring systems. *Wiley Interdisciplinary Reviews: Water*, *8*(3), e1513. https://doi.org/10.1002/wat2.1513

Song, Y., Shi, X., Revil, A., & Kang, X. (2022). Monitoring in-situ microbial growth and decay in soil column experiments by induced polarization. *Geophysical Research Letters*, *49*(16), e2021GL097553. https://doi.org/10.1029/2021GL097553

Stauffer, D., & Aharony, A. (2018). *Introduction to percolation theory*. Taylor & Francis. https://doi.org/10.1201/9781315274386

Sun, Z., Mehmani, A., & Torres-Verdín, C. (2021). Pore-scale investigation of the electrical resistivity of saturated porous media: Flow patterns and porosity efficiency. *Journal of Geophysical Research: Solid Earth*, *126*(12), e2021JB022608. https://doi.org/10.1029/2021JB022608

Tercier, P. E. (1992). *Electrical resistivity of partially saturated sandstones*. University of British Columbia. https://doi.org/10.14288/1.0052893

Toms, J., Müller, T., Ciz, R., & Gurevich, B. (2006). Comparative review of theoretical models for elastic wave attenuation and dispersion in partially saturated rocks. *Soil Dynamics and Earthquake Engineering*, *26*(6–7), 548–565. https://doi.org/10.1016/j.soildyn.2006.01.008

Tso, C. H. M., Kuras, O., & Binley, A. (2019). On the field estimation of moisture content using electrical geophysics: The impact of petrophysical model uncertainty. *Water Resources Research*, *55*(8), 7196–7211. https://doi.org/10.1029/2019WR024964

Tzimas, G., Matsuura, T., Avraam, D., Van der Brugghen, W., Constantinides, G., & Payatakes, A. (1997). The combined effect of the viscosity ratio and the wettability during forced imbibition through nonplanar porous media. *Journal of Colloid and Interface Science*, *189*(1), 27–36. https://doi.org/10.1006/jcis.1996.4658

Wang, H., & Revil, A. (2020). Surface conduction model for fractal porous media. *Geophysical Research Letters*, *47*(10), e2020GL087553. https://doi.org/10.1029/2020GL087553

Waxman, M. H., & Smits, L. (1968). Electrical conductivities in oil-bearing shaly sands. *Society of Petroleum Engineers Journal*, *8*(02), 107–122. https://doi.org/10.2118/1863-A

Wei, J.-Z., & Llle, O. B. (1991). Influence of wettability on two-and four-electrode resistivity measurements on Berea sandstone plugs. *SPE Formation Evaluation*, *6*(04), 470–476. https://doi.org/10.2118/21628-PA

Weller, A., Slater, L., & Nordsiek, S. (2013). On the relationship between induced polarization and surface conductivity: Implications for petrophysical interpretation of electrical measurements. *Geophysics*, *78*(5), D315–D325. https://doi.org/10.1190/geo2013-0076.1

Yang, W., Brownlow, J. W., Walker, D. L., & Lu, J. (2021). Effect of surfactant-assisted wettability alteration on immiscible displacement: A microfluidic study. *Water Resources Research*, *57*(8), e2020WR029522. https://doi.org/10.1029/2020WR029522

Yang, Z., Shao, C., Zhou, G., & Qiu, C. (2007). Modeling non-aqueous phase liquid displacement process. *Petroleum Science*, *4*(3), 40–46. https://doi.org/10.1007/s12182-007-0007-8

Zhang, J., Zhang, H., Lee, D., Ryu, S., & Kim, S. (2020). Microfluidic study on the two-phase fluid flow in porous media during repetitive drainage-imbibition cycles and implications to the CAES Operation. *Transport in Porous Media*, *131*(2), 449–472. https://doi.org/10.1007/s11242-019-01353-4

Zimmermann, E., Kemna, A., Berwix, J., Glaas, W., Münch, H., & Huisman, J. (2008). A high-accuracy impedance spectrometer for measuring sediments with low polarizability. *Measurement Science and Technology*, *19*(10), 105603. https://doi.org/10.1088/0957-0233/19/10/105603